Physics potential of timing layers for future detectors

C.-H. Yeh[a], S.V. Chekanov[b], A.V. Kotwal[c], N.V. Tran[d], S.-S. Yu[a]

[a] *Department of Physics and Center for High Energy and High Field Physics, National Central University, Chung-Li, Taoyuan City 32001, Taiwan*
[b] *HEP Division, Argonne National Laboratory, 9700 S. Cass Avenue, Argonne, IL 60439, USA.*
[c] *Department of Physics, Duke University, USA*
[d] *Fermi National Accelerator Laboratory*

Abstract

Keywords:

1. Introduction

Future experiments, such as CLIC [**?**], International Linear Collider (ILC) [**?**], high-energy LHC (HE-LHC), future circular *pp* colliders of the European initiative, FCC-hh [**?**] and the Chinese initiative, SppC [**?**] will require high precision measurements of particle and jets at large transverse momenta. The usage of timing information for such experiments can provide additional information that can be used to improve particle and jet reconstruction, as well as to deal with background events. At this moment, conceptional design reports for these experiments did not fully explore the benefits of the time of flight (TOF) measurements with tens-of-picosecond resolutions.

2. Proposal

A generic design of hadronic (electromagnetic) calorimeters for future particle collision experiments (HE-LHC, FCC, CLIC, ILC etc.) is based on two main characteristics: (1) high-granularity calorimeters with cells ranged from 3×3 mm^2 (for ECAL) to 5×5 cm^2 (for HCAL) in sizes. (2) timing with nanosecond precision that improves background rejection, vertex association, and detection of new particles. According to the CPAD report [**?**], a development of picosecond time resolution for future calorimeters is one of the critical needs. Presently. high-granularity calorimeters (with ¿1 millions channels) with tens of picoseconds resolution represent a significant challenge due the large cost.

As a part of the HL-LHC upgrade program, CMS and ATLAS experiments are designing high-precision timing detectors with the time resolution of about 30 ps. They are based on silicon sensors that add an extra "dimension to event reconstruction. Such timing capabilities are not fully explored for future detectors beyond the HL-LHC

Email addresses: a9510130375@gmail.com (C.-H. Yeh), chekanov@anl.gov (S.V. Chekanov), ashutosh.kotwal@duke.edu (A.V. Kotwal), ntran@fnal.gov (N.V. Tran), syu@cern.ch (S.-S. Yu)

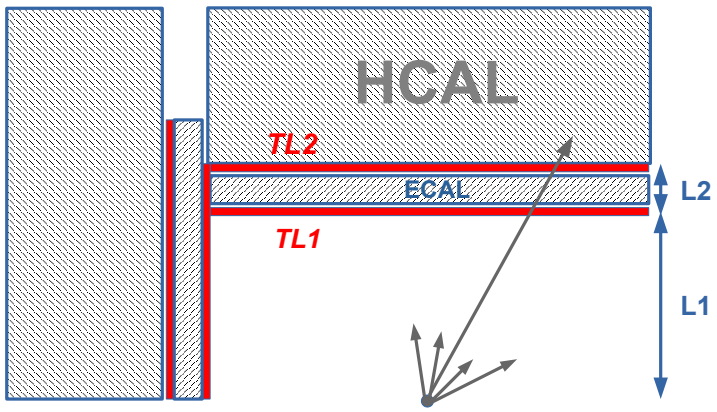

Figure 1: An example of positions of the timing layers for a generic detector. ADD TEXT

upgrade. High-precision timing will be beneficial for new physics searches and b-tagging for all post-LHC experiments. For CLIC and FCC, high-precision time stamping will be essential for background rejection and pile-up mitigation.

Currently, the baseline designs of the high-granularity ECAL and HCAL of the CLIC/FCC detectors have not been optimized for precision timing in the range of a few tens of picoseconds. The latter is considered as an expensive option for many mullions of channels of these high-granularity detectors. This opens an opportunity to investigate a cost-effective timing layer (with the time resolution of smaller than 30 ps) for the post-LHC detectors. This layer will be installed on front of high-granularity calorimeters, covering both the forward and barrel regions.

In this paper we will investigate physics advantages for timing layers in the front of calorimeters (sometime termed pre-shower detector) of the post-LHC experiments. This timing detector will have a similar granularity as the proposed high-granularity EM calorimeters themselves, but will have a sensor technology and readout which is best suited for mip time stamping (not necessarily for energy reconstruction). Our proposal is to enclose the EM detectors with two timing layers, one - before the first EM layer, and the second is after the last EM layer (but before the HCAL). The two layers of the timing detector allows a robust identification of time by correlating the position and timestamps of the particle passing through the ECAL.

In this paper we will explore this idea using full Monte Carlo simulations. A schematic representation of the positions of the timing layers for a generic detector geometry is shown in Fig. 1

The second layer of the timing detector can only be justified if fluctuations of hits

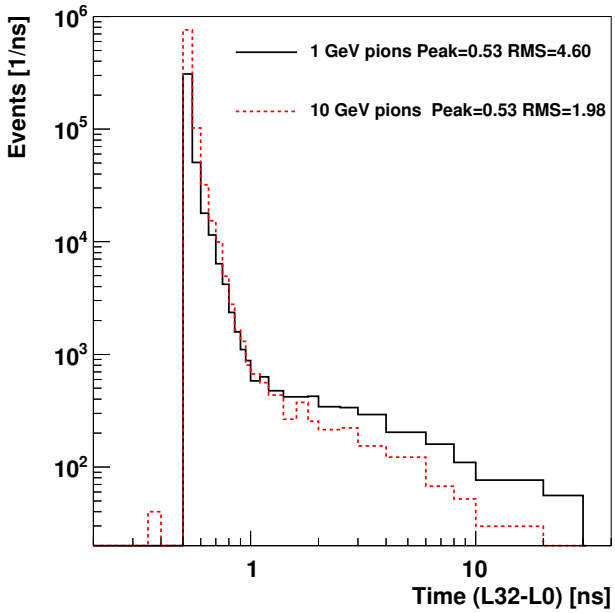

Figure 2: The difference between time of hits between the last and first layer of ECAL for single pions with the transverse momentum 1 and 10 GeV. Only first (fastest) hits were considered

times are smaller than the resolution of the timing layers. In oder to verify this, we used a full Geant4 (version 10.3) [**?**] simulation of the SiFCC detector [**?**] that allows to use the information on hits from the ECAL. The ECAL is built from a highly segmented silicon-tungsten with the transverse cell size of 2×2 cm. The ECAL has 30 layers built from tungsten pads with silicon readout, corresponding to 35 X_0. The first 20 layers use tungsten of 3 mm thickness. The last ten layers use tungsten layers of twice the thickness, and thus have half the sampling fraction.

To verify that the time differences between last and first layer of ECAL is sufficiently small, and can be neglected for the timing layers that have a timing resolution of the order of 10 ns, a sample of single pions was created with 1 and 10 GeV. The particles were reconstructed in the ECAL calorimeter, and the time difference $\Delta T = T_{\text{last}} - T_{\text{first}}$ of the hits between the last and first ECAL layers was calculated. Only hits that arrive first were considered. Figure 2 shows the time distribution for 1 and 10 GeV pions. It can be seen that the peak positions of the distributions are smaller than 1 GeV, as expected for the distance of about 20 cm between the last and first layers[1]. More importantly, the RMS of these distributions are significantly smaller than the 10 ns. Therefore, for the timing layers that have a resolution of the order of 10-20 ns, a single particle crossing the two layers will be seen a single simultaneous hit, thus such hits can be well correlated in time and identified as a single crossing particle.

[1]The precision with which the simulations were performed are about 0.2-0.3 ns

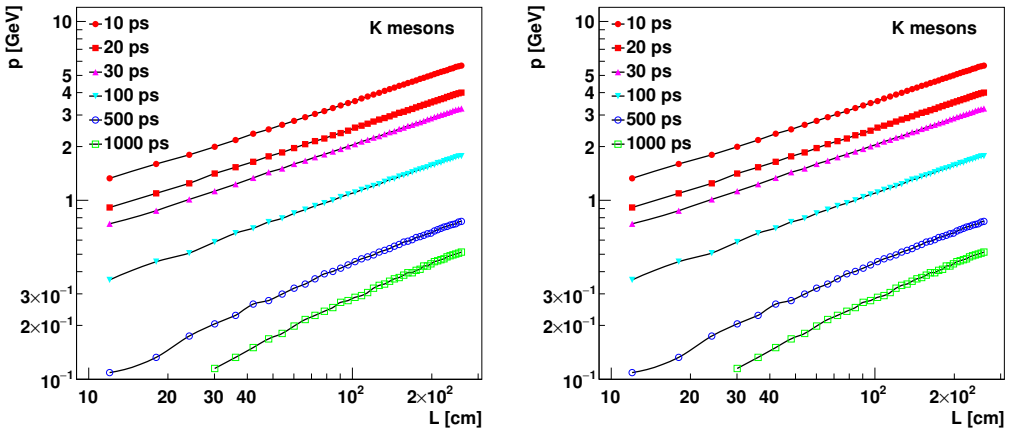

(a) (b)

Figure 3: The 3σ separation from the pion mass.. ADD TEXT

3. Single particles

Before considering the full Geant4 simulation, let us discuss the benefit of the TOF information for identification of separate particles. Fig. 3 shows the 3σ separation from the pion mass hypothesis using the same technique as discussed in [**?**]. The lines are calculated using the following consideration: ADD TEXT

4. Timing layers for single particles

5. Timing layers for FCC and jets

In the previous sections, the capability of the timing among the various resolutions of the detector used on distinguishing the different kinds of single particle that has the different mass, momentum as well as the length of going through the detector is well-investigated as the excellent variable within the three sigma hypothesis. The next necessary step is to employ the timing, which is the potential method of discriminating the different number of the subjets in a large radius jet as well, into tackling the intractable dilemma that has been being concerned about on the highly-boosted circumstances resulting in the particles of the jet are too close to each other, and the truth number of the subjet could be misestimated, along with impacting on the analysis in the future dramatically.

The simplified-cases simulating the pileup-free conditions with the already-known processes are involved in these studies under the environment of a very-high-energy collider will be explored as the benchmark of the timing applied in the future. The same processes of Z'→qq(Background), Z'→WW(Signal) with 5, 10, 20 and 40TeV center-of-mass energy(C.M.) as the ones exploited in our second paper, are taken into account as the targets of doing the researches on the same matter with the timing implemented.

In terms of digging out the potential of the timing, several studies have been done trying on a couple of variables to see whether the timing can give us another degree of information helping on having the improvement on the issue in addition to the P_T that we could obtain directly from the detector . The ΔR, which is the common variable that has been being used in the collider as acquiring the angle between two particles/-jets, is found to be the possible one that can take advantage of using the timing to analyze the structure of the jets more evidently. Also, the ideal cases of separating the different particles with the help of the timing are also premeditated.

The two sets of the collections of the data including both of the generator level(truth-level) and the reconstruction level(reco-level) are utilized in the studies for the purpose of corresponding between each other as the benchmark of the parameters that are found beneficial. At the first place, the definition of many terms applied in the studies will be well-defined as a favor of proceeding smoothly. The second one is to make use of the truth-level information of the four momenta for each particle to figure out the anticipation of the timing being capable of helping on the issue at best ideally. Last but not least, the well-established cases illustrated by using the reco-level information of the non-smearing four momenta and the fastest-response timing[2] from each cell of the calorimeter will be given as the true cases we could expect in our life when the time

[2] As a matter of fact that the detector can response to the first-arrival particle barely in one event, the timing observed from the reco-level can merely be treated as the part of the jet but not the whole one. Oppositely, the particles of the four momenta from a jet can be explicitly known from the information of the truth-level, the timing of each particle should be well-calculated with the formula of the timing listed in the following sections as the ideal cases.

of the timing-capable detector installed in the collider with the very high C.M. energy comes.

5.1. The definitions of the terms introduced in the following studies

In case for avoiding being confused by the terms applied in these studies, predefining for those terms is essential.

5.1.1. The timing used in the truth-level cases

At the first place, the definition of the timing should be obtained as our benchmark to do these studies when dealing with the truth-level information. The standard formula of the timing is as follows for each particle:

$$Timing = \frac{L(\eta)}{V(V_x, V_y, V_z)} \tag{1}$$

Basically, it is the normal formula of the time of flight(TOF), depending on the different η, leading to the different distances L between collision point and HCAL barrel, along with the three-dimensional velocities V of the particles.

But, since the effect of the magnetic field is taken into account, the timing applied in this paper is the modified one with only considering the Z direction of the distance and velocity, and then we can get more precise value of the timing by the truth of the Z-direction trace of the particle isn't changed by the magnetic field. The formula used in this paper is as follows:

$$Timing = \frac{L_z}{V(V_z)} \tag{2}$$

After applying this formula on all particles, and the timing can be obtained without the bending effect coming from the magnetic field.

5.1.2. The trailing particles applied in all cases

The another terms should be noticed as the important ones are two sorts of the trailing particles applied in all cases. The definition of the trailing particles defined by the Timing(T) and transverse momentum(PT) should be clarified. We have two categories of the trailing particles

1. Defined by the T, so-called "trailing-T", meaning that the particle has the longest traveling timing in the jet.
2. Defined by the PT, so-called "trailing-PT", meaning that the lowest-PT particle in the jet.

Logically, we can define next-to trailing particle as well, such as the second long traveling timing-"next-to-trailing-T" or the second low PT-"next-to-trailing-PT", and so on.

5.2. The truth-level cases

When coming up with any new variable, the truth-level information can be utilized as the outpost with the guardian monitoring on the variables could be useful or not without the joint of the particle-showering effect involved in at the reco-level . In this section, the truth-level information will be adopted as the one to aim to inspect the power of the variable found out within the a number of the studies.

In order to compare the studies carried out by the truth-level information with the ones done at the reco-level, the selection of the events at the generator level should be enlightened at first. At the first place, since the information of the four momenta upon the particles reconstructed by HCAL barrel in SiFCC will be utilized as the candidates of excavating the potential of the timing, the pre-selection of the eta on the particles should be aligned with the HCAL which is in the region of . Subsequently, the effect of the magnetic field should be concerned as the probably authentic situation occurring in the collider. With the calculations played out by , the cut down limit of the energy owned by the particles is about 1.5GeV.

Figure**??** and **??** show some of the distributions of ΔR, which are the angles between the leading-PT particle as well as five kinds of the trailing-T and trailing-PT particles, demonstrated by the 5TeV and 40TeV cases individually as two patterns explaining on the discriminations. By comparing between these two collections, the effect of the timing to discern the jets containing the various number of the subjets is displayed off obviously. For the distributions of the WW samples, the broader ones ranging from 0 to 0.2 compared with the QQ samples can be easily recognized in both cases.

Instead of the flat-like distributions as WW cases, the energy-dependent discrimination with the WW distributions can be acquainted from the figures conspicuously. The lower energy case of 5TeV shown in Fig**??** shows the similar shape as the QQ cases but concentrating in the smaller region. Significantly, the higher energy case of 40TeV demonstrated in Fig**??** displays the very narrow distributions centralizing near the 0, which is considerably distinctive from the WW cases, can be the proof of ΔR is the great variable for the issue. After showing the separation power of ΔR with the histograms qualitatively, the quantitive way with the module of the Boosted Decision Tree(BDT) will be utilized as investigating the power of the discrimination for all energies.

In the Fig**??**, the BDT method is applied to make out the efficiency of separating the two processes with the input variables of those five trailing particles defined by T and PT as mentioned in the previous paragraph for all four energies. The statement which can be addressed from the plots is that the separation power of the timing with PT is as perfect as T, originating from the lines in the plots overlap together. In this case, the variable is worthy for us to keep exploring on to see whether the cases are similar as the ones done with the reco-level data.

With regard to taking advantage of the timing ideally, the other one is to take it as the tool of identifying the particles. The plots of Fig**??** and Fig**??** show the

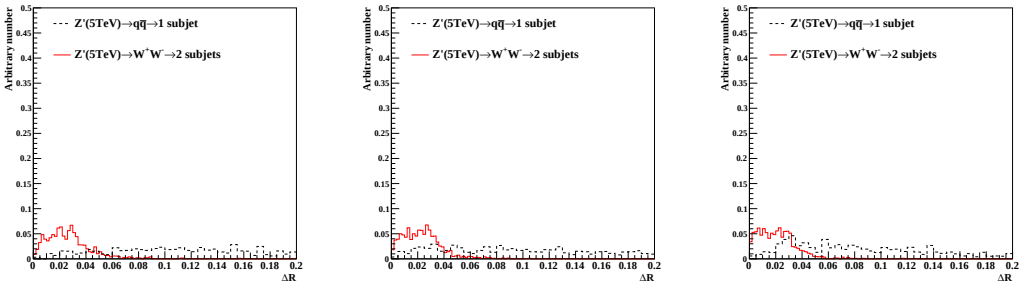

(a) 20×20 cm^2 (b) 5×5 cm^2 (c) 1×1 cm^2

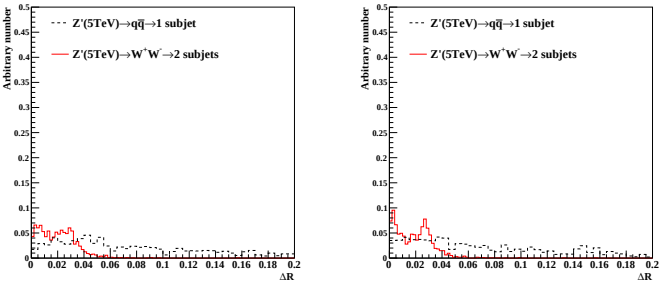

(d) 1×1 cm^2 (e) 1×1 cm^2

Figure 4: Distributions of τ_{21} for $M(Z') = 20$ TeV for different detector granularities. Cell sizes of 20×20, 5×5, and 1×1 cm^2 are shown here.

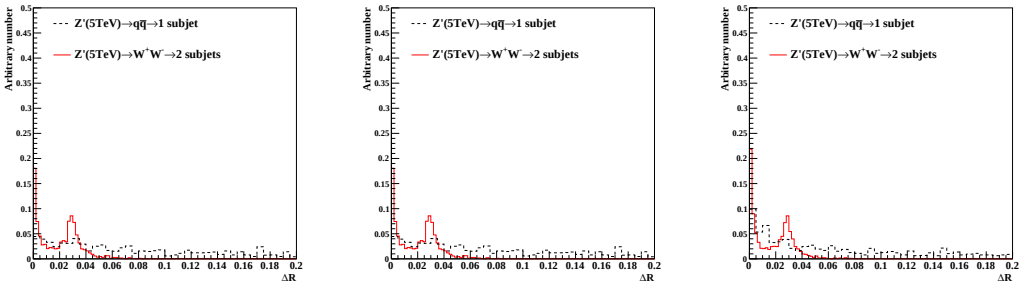

(a) 20×20 cm^2 (b) 5×5 cm^2 (c) 1×1 cm^2

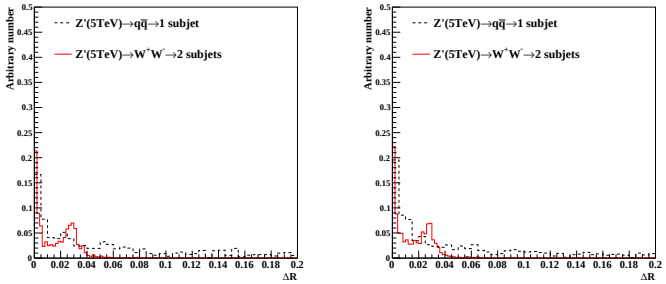

(d) 1×1 cm^2 (e) 1×1 cm^2

Figure 5: Distributions of τ_{21} for $M(Z') = 20$ TeV for different detector granularities. Cell sizes of 20×20, 5×5, and 1×1 cm^2 are shown here.

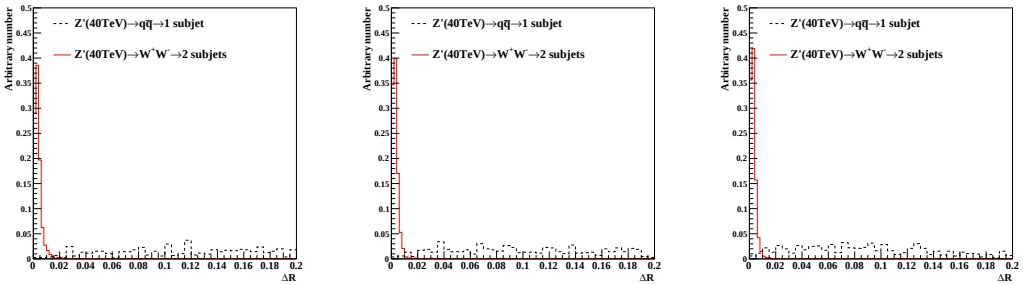

(a) 20×20 cm^2 (b) 5×5 cm^2 (c) 1×1 cm^2

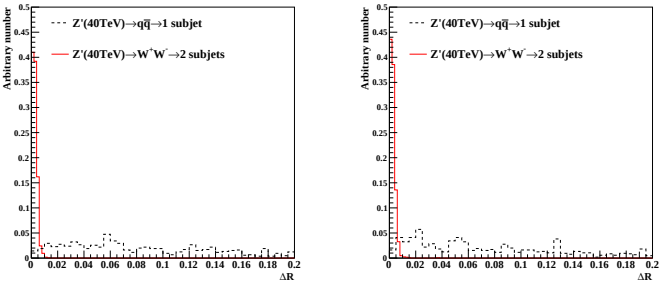

(d) 1×1 cm^2 (e) 1×1 cm^2

Figure 6: Distributions of τ_{21} for $M(Z') = 20$ TeV for different detector granularities. Cell sizes of 20×20, 5×5, and 1×1 cm^2 are shown here.

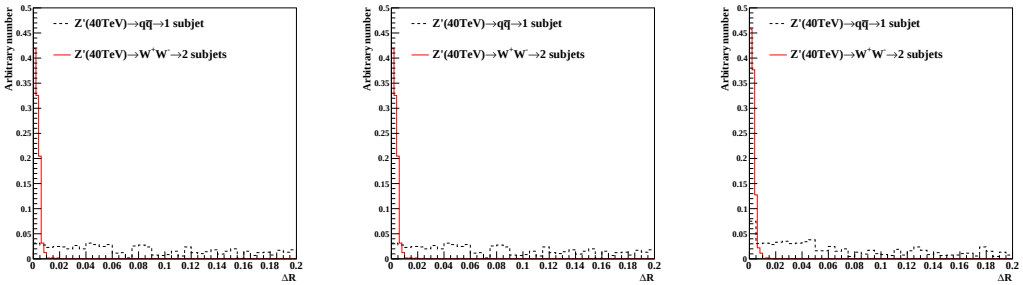

(a) 20×20 cm^2 (b) 5×5 cm^2 (c) 1×1 cm^2

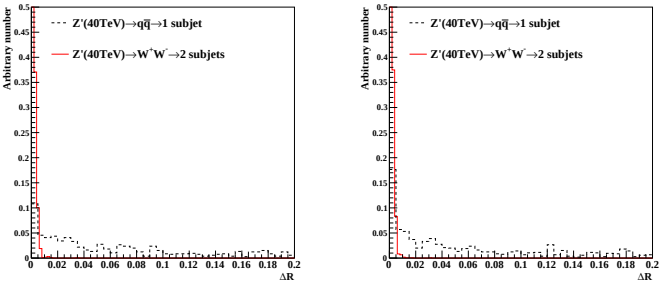

(d) 1×1 cm^2 (e) 1×1 cm^2

Figure 7: Distributions of τ_{21} for $M(Z') = 20$ TeV for different detector granularities. Cell sizes of 20×20, 5×5, and 1×1 cm^2 are shown here.

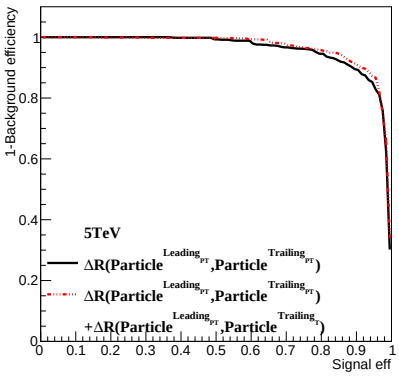

(a) 20×20 cm^2

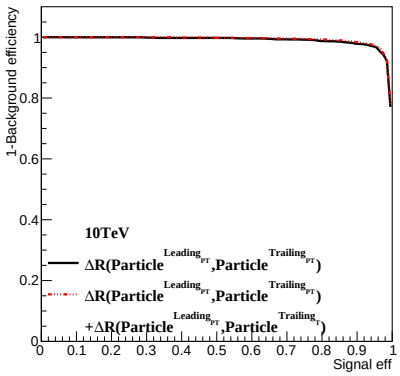

(b) 5×5 cm^2

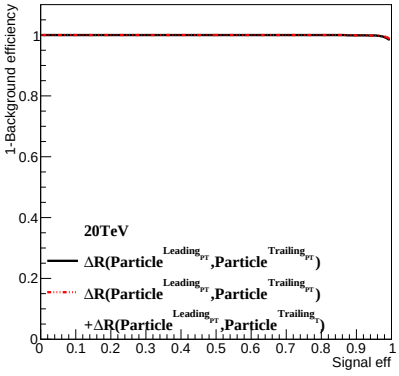

(c) 1×1 cm^2

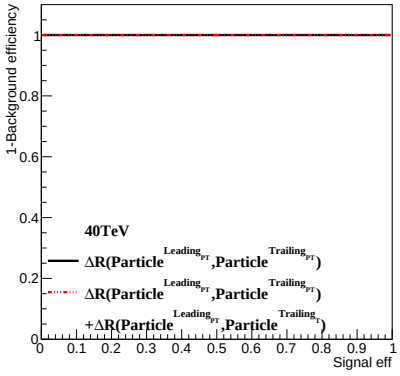

(d) 1×1 cm^2

Figure 8: Distributions of τ_{21} for $M(Z') = 20$ TeV for different detector granularities. Cell sizes of 20×20, 5×5, and 1×1 cm^2 are shown here.

distribution of the particle ID with respect to the trailing-PT and trailing-T cases, the another function found favorable is that the protons can be tagged more within the cases of the Trailing-T. For the purpose of quantifying them, we manage

5.3. The Reco-level cases

Over the specific studies for the DeltaR with the truth information in the former section, the capability of the DeltaR is aware of as a a great variable as the P_T into investigating the different number of the subjets within a large radius jet. Followed up by that, the essential step of verifying on the efficiency of the variable applied in the real case is to prepare the reco-level data, which is served as the situations operating in the future, to corroborate the advanced of the timing employed into handling the issue.

The distributions of the DeltaR, which are revealed in the Fig**??** and Fig**??** for 5TeV and 40TeV as the examples of two extreme cases in this study, show that the distributions of WW and QQ can't be well-separated by both parameters sharply at the higher C.M. points compared with the truth-level which is caused by the non-smearing detector resulting in the same-angle-effect meaning the deltaR can only be the angle of four momenta between the calojet but not the authentic truth particles . Surprisingly, the timing in this case can give us a little bit improvement upon the P_T cases with the proof of the BDT plots in Fig.**??** summarizing the efficiency of those variables. The much improvement with the timing can be observed at the higher C.M. point.

Speaking of the deltaR which is strongly-dependent of the precise of measuring the momenta, the tracker, which can get rid of the issue on non-smearing problem as ECAL to explicitly measure the momentum with the high-granularity cell, is the essential detector to explore the efficiency of the parameter. The distributions of DeltaR with the tracker are posted in Fig.**??**, that show the cases are very similar to the truth-level ones as if the precise four momenta can be be sought, the higher separation between two different number of subjets can be discovered. As the schemes of BDT plots shown in Fig.**??** and Fig.**??** as the ones mentioned in the previous paragraph, the lines obtained from the tracker with the trailing-PT arrangement show that the high-rejection of the background with the accurate measurement of the four momenta can be used as the mean to nail down the task of distinguishing the different number of subjet. [3]

[3] At the moment, since the timing information from the tracker in our current simulation can't be acquired as another detectors, we only apply the PT-trailing for the tracker case.

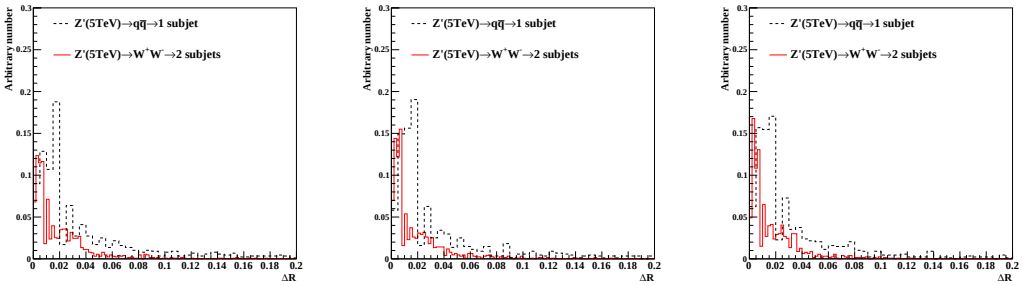

(a) 20×20 cm^2 (b) 5×5 cm^2 (c) 1×1 cm^2

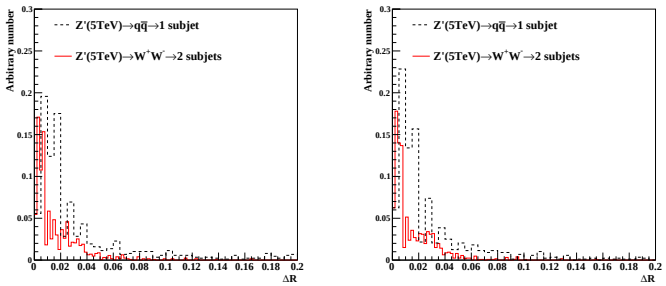

(d) 1×1 cm^2 (e) 1×1 cm^2

Figure 9: Distributions of τ_{21} for $M(Z') = 20$ TeV for different detector granularities. Cell sizes of 20×20, 5×5, and 1×1 cm^2 are shown here.

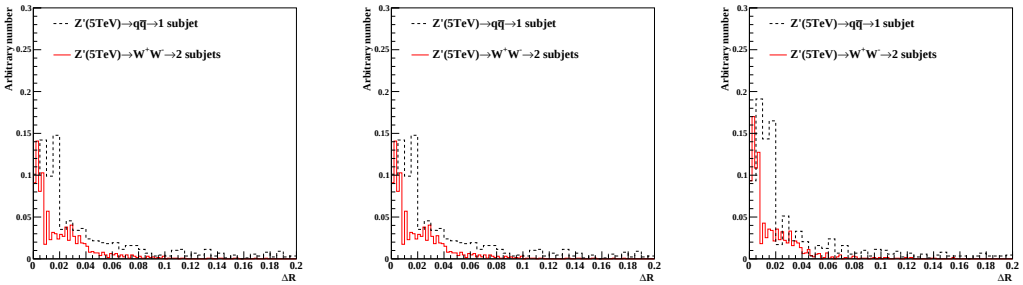

(a) 20×20 cm^2 (b) 5×5 cm^2 (c) 1×1 cm^2

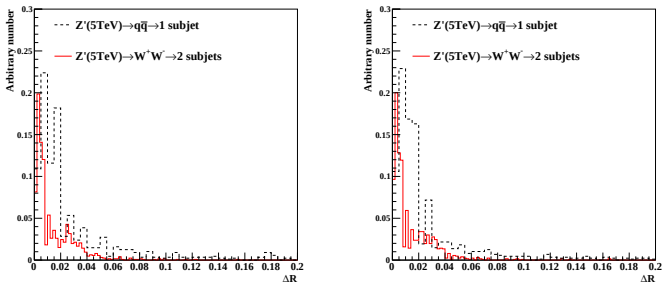

(d) 1×1 cm^2 (e) 1×1 cm^2

Figure 10: Distributions of τ_{21} for $M(Z') = 20$ TeV for different detector granularities. Cell sizes of 20×20, 5×5, and 1×1 cm^2 are shown here.

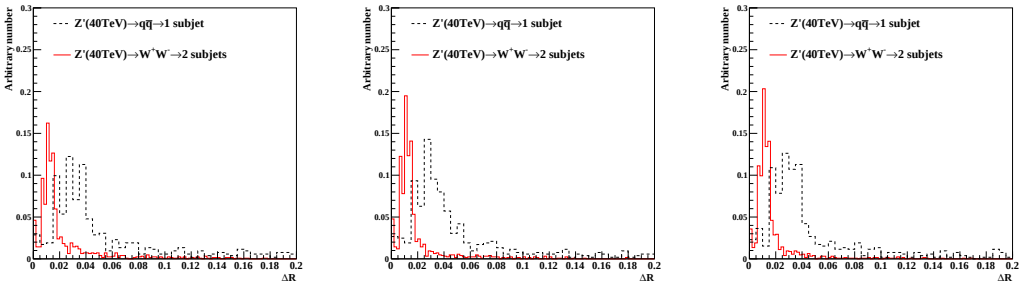

(a) 20×20 cm^2 (b) 5×5 cm^2 (c) 1×1 cm^2

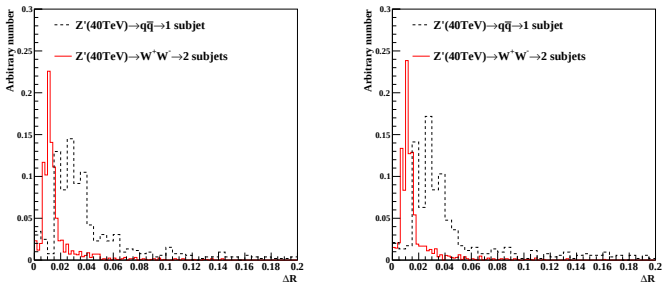

(d) 1×1 cm^2 (e) 1×1 cm^2

Figure 11: Distributions of τ_{21} for $M(Z') = 20$ TeV for different detector granularities. Cell sizes of 20×20, 5×5, and 1×1 cm^2 are shown here.

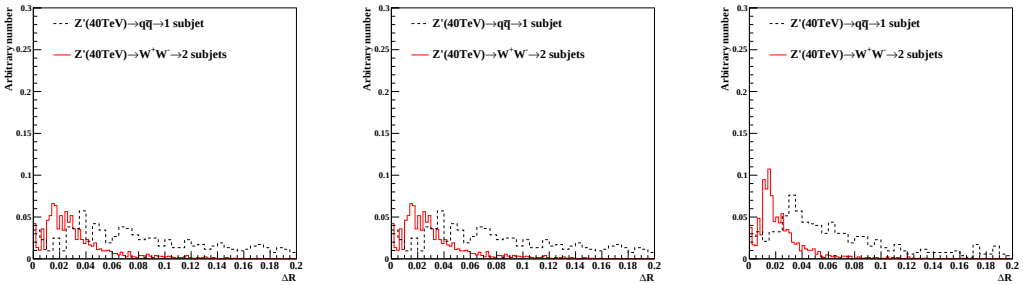

(a) 20×20 cm^2 (b) 5×5 cm^2 (c) 1×1 cm^2

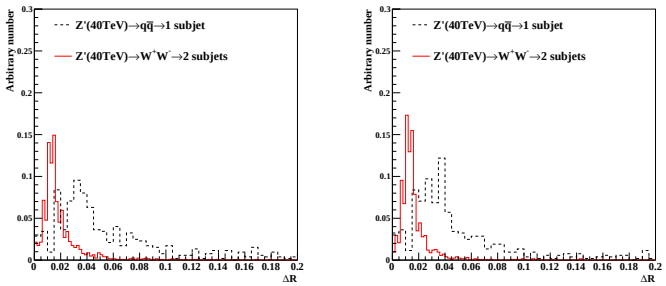

(d) 1×1 cm^2 (e) 1×1 cm^2

Figure 12: Distributions of τ_{21} for $M(Z') = 20$ TeV for different detector granularities. Cell sizes of 20×20, 5×5, and 1×1 cm^2 are shown here.

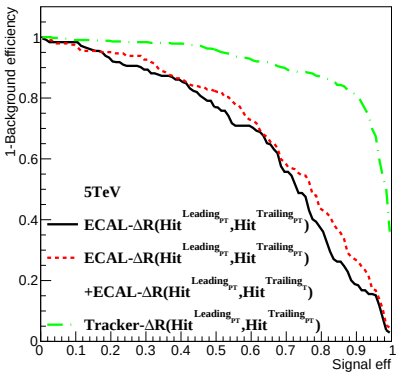

(a) 20×20 cm^2

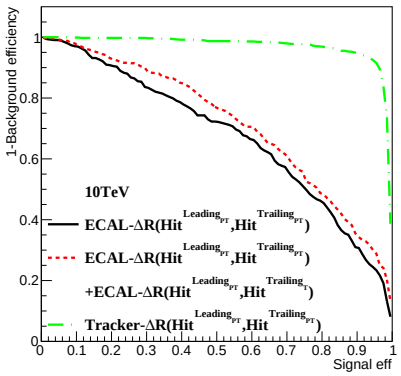

(b) 5×5 cm^2

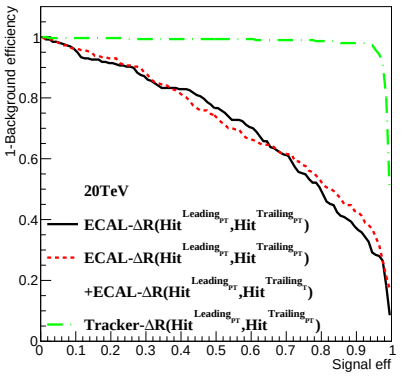

(c) 1×1 cm^2

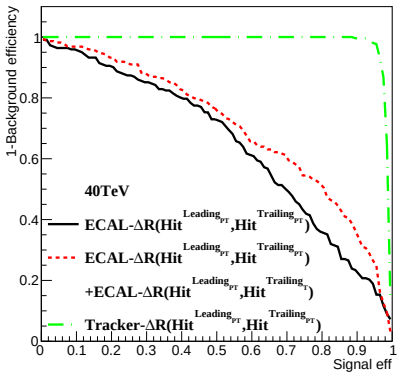

(d) 1×1 cm^2

Figure 13: Distributions of τ_{21} for $M(Z') = 20$ TeV for different detector granularities. Cell sizes of 20×20, 5×5, and 1×1 cm^2 are shown here.

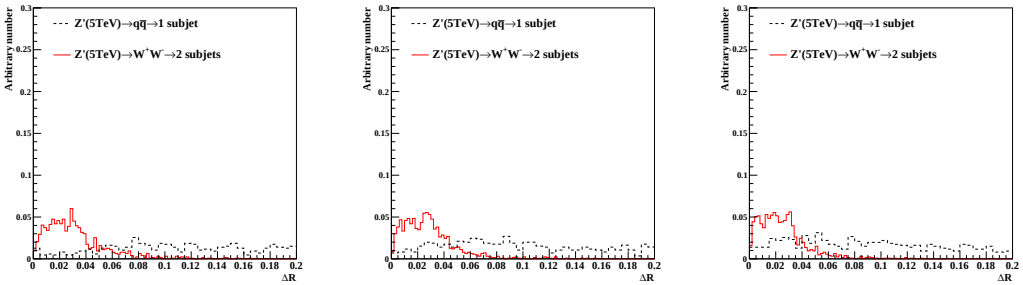

(a) 20×20 cm^2 (b) 5×5 cm^2 (c) 1×1 cm^2

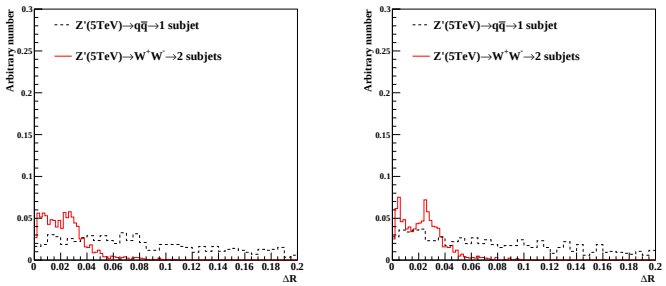

(d) 1×1 cm^2 (e) 1×1 cm^2

Figure 14: Distributions of τ_{21} for $M(Z') = 20$ TeV for different detector granularities. Cell sizes of 20×20, 5×5, and 1×1 cm^2 are shown here.

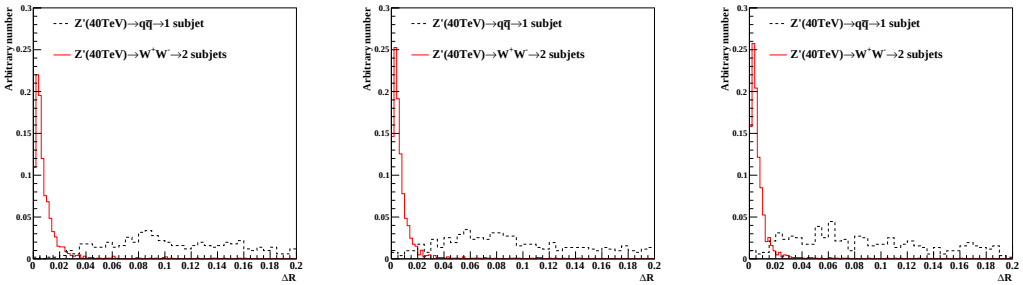

(a) 20×20 cm^2 (b) 5×5 cm^2 (c) 1×1 cm^2

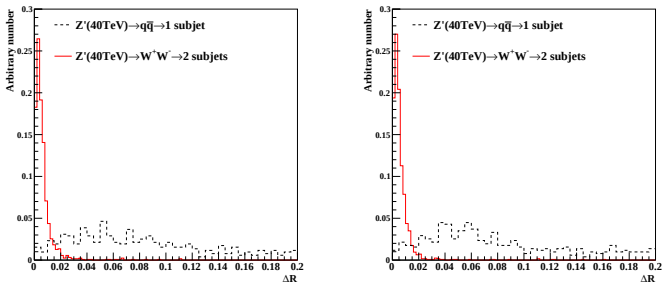

(d) 1×1 cm^2 (e) 1×1 cm^2

Figure 15: Distributions of τ_{21} for $M(Z') = 20$ TeV for different detector granularities. Cell sizes of 20×20, 5×5, and 1×1 cm^2 are shown here.